Nonlocal Elasticity Yields Equilibrium Patterns in Phase Separating Systems

Yicheng Qiang, Chengjie Luo, and David Zwicker*

Max Planck Institute for Dynamics and Self-Organization, Am Faßberg 17, 37077 Göttingen, Germany

(Received 1 August 2023; revised 16 December 2023; accepted 5 March 2024; published 12 April 2024)

Recent experiments demonstrated the emergence of regular mesoscopic patterns when liquid droplets form in an elastic gel after cooling. These patterns appeared via a continuous transition and were smaller in stiffer systems. We capture these observations with a phenomenological equilibrium model describing the density field of the elastic component to account for phase separation. We show that local elasticity theories are insufficient, even if they allow large shear deformations. Instead, we can account for key observations using a nonlocal elasticity theory to capture the gel's structure. Analytical approximations unveil that the pattern period is determined by the geometric mean between the elastocapillary length and a nonlocality scale. Our theory highlights the importance of nonlocal elasticity in soft matter systems, reveals the mechanism of this mesoscopic pattern, and will improve the engineering of such systems.

DOI: 10.1103/PhysRevX.14.021009 Subject Areas: Soft Matter

I. INTRODUCTION

Phase separation in elastic media is a ubiquitous phenomenon, which is relevant in synthetic systems to control micropatterning [1–3] and in biological cells, where droplets are embedded in the elastic cytoskeleton or chromatin [4–6]. While biological systems are typically dynamic and involve active processes, the simpler synthetic systems can exhibit stable regular structures. These patterns harbor potential for metamaterials and structural color, particularly since they are easier to produce and manipulate than alternatives like self-assembly by block copolymers [7] or chemical cross-linking [8]. In these applications, it is crucial to control the length scale, the quality, and the stability of the pattern.

Recent experiments found stable regular mesoscopic patterns and demonstrated remarkable control over these structures [1]. However, the mechanism underlying their formation is unclear, complicating further optimization. The experiment proceeds in two steps [Fig. 1(a)] [1]. First, a polydimethylsiloxane gel is soaked in oil at high temperatures for tens of hours until the system is equilibrated. When the temperature is lowered in the second step, the sample develops bicontinuous structures, reminiscent of spinodal decomposition. However, in contrast to spinodal decomposition, the length scale of the structure does not coarsen but stays arrested at roughly 1–10 μm, depending on the gel's stiffness. Interestingly, this transition is reversible and the pattern disappears upon reheating, suggesting a continuous phase transition. Moreover, the resulting pattern is independent of the cooling rate, in contrast to earlier experiments on similar materials [3,9]. Consequently, the experiments might be explainable by an equilibrium theory that captures elastic deformations in the polydimethylsiloxane gel due to oil droplets formed by phase separation.

The experimental observations are reminiscent of microphase separation, e.g., observed in block copolymers [11,12] and interpenetrating polymer networks [13,14]. However, phase transitions in such models are typically first order, e.g., in the seminal Ohta-Kawasaki model [15]. Moreover, in these theories, the size of the involved molecules is similar to the size of the patterns they form, whereas the patterns in the experiment are much larger than the oil molecules and the typical mesh size of the elastic gel [1]. Alternatively, spinodal decomposition of a phase separating system augmented with elasticity might describe the experiments [1]. However, typical local elasticity theory can only account for slowed coarsening [16,17], and we will show that it does not yield stable equilibrium patterns. Consequently, these conventional models cannot explain the qualitative features of the experiments.

In this paper, we propose an equilibrium theory that explains the experimental observations [1]. Using a phenomenological approach, we describe the system by a continuous density field of the elastic component to describe phase separation and elastic deformations with a single free energy. We show that local elastic theories, based on the deformation gradient tensor, cannot account for equilibrium patterns. Consequently, we consider a

*david.zwicker@ds.mpg.de

higher order of the phenomenological approximation, yielding a nonlocal elasticity theory that takes into account the structure of the gel [18–22]. We find a continuous phase transition to a mesoscopic patterned phase, consistent with experimental observations. We predict that the equilibrium period is governed by the geometric mean between the elastocapillary length and the nonlocality scale, which captures the stiffness dependence of the experimentally observed pattern length scale.

II. RESULTS

We aim to explain the experimental results [1] using a phenomenological equilibrium theory for an isothermal system. We thus define a free energy comprising entropic and enthalpic contributions that can induce phase separation as well as contributions from elastic deformation. While the former contributions can be captured by the volume fraction density $\phi(\boldsymbol{x})$ defined in lab coordinates $\boldsymbol{x}$, deformations are described by the deformation gradient tensor $\boldsymbol{F}(\boldsymbol{X}) = \mathrm{d}\boldsymbol{x}/\mathrm{d}\boldsymbol{X}$, which quantifies how material points at position $\boldsymbol{x}$ have been moved from the reference positions $\boldsymbol{X}$ where the gel is undeformed. Note that volume conservation implies $\det(\boldsymbol{F}) = \phi_0/\phi$, where ϕ_0 denotes the fraction in the relaxed homogeneous initial state [16].

A. Local elasticity models cannot explain periodic equilibrium patterns

We start by investigating a broad class of elastic models, where the elastic energy density is only a function of the deformation gradient tensor $\boldsymbol{F}$. The free energy F of the entire system can then be expressed as

$$F_{\mathrm{local}}[\boldsymbol{F},\phi] = \frac{k_{\mathrm{B}}T}{\nu}\int [f_{\mathrm{el}}(\boldsymbol{F}) + f_0(\phi) + \kappa|\boldsymbol{\nabla}\phi|^2]\mathrm{d}\boldsymbol{x}, \qquad (1)$$

where k_{B} is Boltzmann's constant, T is the constant absolute temperature of the system, and ν is a relevant molecular volume, e.g., of the solvent molecules. In the integral, the first term captures the elastic energy, f_0 accounts for molecular interactions and translational entropy associated with ordinary phase separation, while the last term proportional to the positive parameter κ penalizes volume fraction gradients, thus causing surface tension [23,24]. Equilibrium states then correspond to functions $\phi(\boldsymbol{x})$ and $\boldsymbol{F}(\boldsymbol{X})$ that minimize F_{local} and obey the compatibility constraint and volume conservation.

Can local elasticity models permit periodic equilibrium states? To test this, we assume that such a state, described by periodic functions $\phi^*(\boldsymbol{x})$ and $\boldsymbol{F}^*(\boldsymbol{x})$, exists. We then show that scaling this state by a factor $\lambda > 1$ in all spatial directions, $\phi^*(\lambda^{-1}\boldsymbol{x})$, lowers the free energy F_{local} given by Eq. (1), implying that it could not have been an equilibrium state. While we present the mathematical details in the Supplemental Material [10], the gist of the argument can be seen by considering the free-energy density $\bar{f} = F_{\mathrm{local}}/V$ of a unit cell of volume V of the periodic pattern. Scaling does not affect the contribution of the second integrand in Eq. (1) to $\bar{f}$, precisely because it averages a local function over one period. Similarly, the first integrand stays invariant since the scaling factor λ affects the lab coordinates $\boldsymbol{x}$ and the reference coordinates $\boldsymbol{X}$ equally, so the values of the deformation gradient tensor $\boldsymbol{F} = \mathrm{d}\boldsymbol{x}/\mathrm{d}\boldsymbol{X}$ are invariant and the scaled tensor field reads $\boldsymbol{F}^*(\lambda^{-1}\boldsymbol{x})$. In contrast, the last term contributes less for the scaled pattern since scaling reduces the gradient term to $\lambda^{-1}\boldsymbol{\nabla}\phi^*$, consistent with a lower penalty for shallower interfaces. Taken together, we thus showed that the free energy of any periodic state can be reduced by scaling, implying such states cannot be at equilibrium and instead would eventually evolve toward longer length scales. In essence, this is because only the interfacial parameters κ carries dimensions of length whereas length scales associated with the structural details of the elastic material do not appear in local elastic theories.

B. Mesh structure suggests nonlocal elasticity theory

Realistic elastic meshes exhibit length scales like the mesh size (∼10 nm [22,25,26]) and correlation lengths of spatial heterogeneities (∼100 nm [27–29]), which are comparable to the pattern length scale (several 100 nm to several micrometers [1]). We thus hypothesize that a characteristic length of the mesh is key for explaining the observed patterns. Such a characteristic length can be systematically included in our phenomenological theory by expanding the elastic energy in terms of the displacement field; see Sec. III of the Supplemental Material [10]. This approach generically leads to *nonlocal elasticity theory*, where a nonlocality scale ξ quantifies at what length scale nonlocal effects become relevant [18–22].

The origin of nonlocal elasticity theory can be illustrated in the simple case where the elastic mesh is described as a collection of elastic elements; see Fig. 1(b). These elements can represent either molecules forming the mesh or structures on the larger correlation length scale of heterogeneities. In any case, the elastic elements connect material points separated by a finite distance, implying the stress at a particular material point results from summing over the interactions with all connected material points. Consequently, stresses are never strictly local, and the associated elastic energy cannot be expressed as a local function of the strain. Instead, in a continuous field theory, the nonlocal stress is expressed as a convolution [18,21]. The familiar local elasticity theory then emerges as a limiting case when considering phenomena on scales large to the nonlocality scale ξ.

To develop a simple description of phase separation with nonlocal elasticity, we focus on one-dimensional systems, where the deformation of the elastic mesh is captured by the

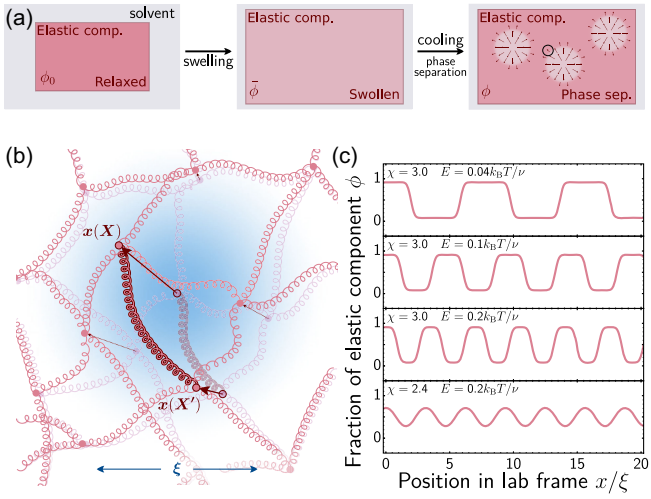

FIG. 1. Nonlocal elasticity yields regular equilibrium patterns. (a) Schematic picture of the experiment [1]: A relaxed elastic gel is swollen in a solvent at high temperature; after cooling, a regular pattern emerges. (b) Schematic of a network of elastic elements (curly lines) connecting material points (red dots). Arrows indicate the displacement of material points from the reference state (transparent, positions $\boldsymbol{X}$) to the deformed state (opaque, positions $\boldsymbol{x}$). The energy of the highlighted elastic element depends on the distance between the two connected points, revealing its nonlocal nature. Coarse graining this system yields the nonlocal convolution kernel (blue density), whose size ξ is roughly given by the length of the elastic elements. Note that the elastic elements need not correspond to molecules, but could capture the interaction of dense mesh regions since realistic meshes are heterogeneous. (c) Equilibrium profiles $\phi(x)$ for various stiffnesses E and interaction parameters χ for $\phi_0 = 1$, $\bar{\phi} = 0.5$, and $\kappa = 0.05\xi^2$. Profiles were obtained by numerically minimizing F_{nonlocal}; see Supplemental Material [10].

scalar strain ϵ, which is directly connected to the only component F_{xx} of the deformation gradient tensor, $\epsilon = F_{xx} - 1$. Volume conservation then implies

$$\epsilon(X) = \frac{\phi_0}{\phi(X)} - 1, \tag{2}$$

where the fraction $\phi(x)$ in the lab frame follows from the coordinate transform $\mathrm{d}x/\mathrm{d}X = \epsilon(X) + 1$. This connection between strain ϵ and volume fraction ϕ permits a theory in terms of only one scalar field in this one-dimensional case. Using a simple linear elastic model for the local stress, $\sigma = E\epsilon$ with elastic modulus E, we obtain the *nonlocal stress*,

$$\sigma_{\text{nonlocal}}(X) = E \int \epsilon(X') g_\xi(X' - X)\mathrm{d}X', \tag{3}$$

where we choose a Gaussian convolution kernel [21,30],

$$g_\xi(X) = \sqrt{\frac{2}{\pi\xi^2}} \exp\left(-\frac{2X^2}{\xi^2}\right), \tag{4}$$

with a characteristic length ξ, which quantifies the nonlocality scale of the mesh [18,21,30]. This nonlocal model can also be derived more rigorously, either generically (see Supplemental Material [10]) or from a more explicit model [18,31]. Note that the convolution is performed in the reference frame since the topology of the network, governing which material points interact with each other, is determined in this unperturbed state. The elastic energy density is then given by the product of strain and nonlocal stress, so the free energy of the entire system reads

$$F_{\text{nonlocal}}[\phi] = \frac{1}{2}\int \epsilon(X)\sigma_{\text{nonlocal}}(X)\mathrm{d}X + \frac{k_B T}{\nu}\int [f_0(\phi) + \kappa(\nabla\phi)^2]\mathrm{d}x, \tag{5}$$

where the first term captures the nonlocal elastic energy expressed in the reference coordinates X, whereas the second term describes the free energy associated with phase separation, expressed in lab coordinates x. We capture the essence of phase separation using a Flory-Huggins model for the local free-energy density [32–34],

$$f_0(\phi) = \phi\log\phi + (1-\phi)\log(1-\phi) + \chi\phi(1-\phi), \tag{6}$$

where $1 - \phi$ is the solvent fraction. Here, the first two terms capture entropic contributions, while the last term describes the interaction between the elastic and solvent component, quantified by the Flory parameter χ. Taken together, Eqs. (2)–(6) define the free energy F_{nonlocal} as a functional of the fraction ϕ of the elastic component.

C. Nonlocal elasticity enables periodic equilibrium patterns

We start by analyzing equilibrium states of the model by determining profiles $\phi(x)$ that minimize F_{nonlocal} using a numerical scheme described in the Supplemental Material [10]. Here, we use the nonlocality scale ξ as the length unit and $k_B T$ as the fundamental unit of energy. Consequently, we consider interfacial parameters $\kappa < \xi^2$ since the interfacial width, which is typically of molecular size, should be smaller than ξ. Our choice of the stiffness E is directly motivated by experimentally measured moduli, which are on the order of 100 kPa. Using these parameters, we find typical macroscopic phase separation, but also periodic patterns for some parameter sets; see Fig. 1(c) herein and Fig. S1 in Supplemental Material [10]. In soft systems (small stiffness E), dilute regions, corresponding to solvent droplets, alternate with dense regions, where the elastic mesh is hardly strained ($\epsilon \ll 1$). In contrast, harmonic profile can emerge for stiff systems (large E). Taken together, the nonlocal elastic theory supports periodic patterns that qualitatively resemble the patterns observed in experiments [1].

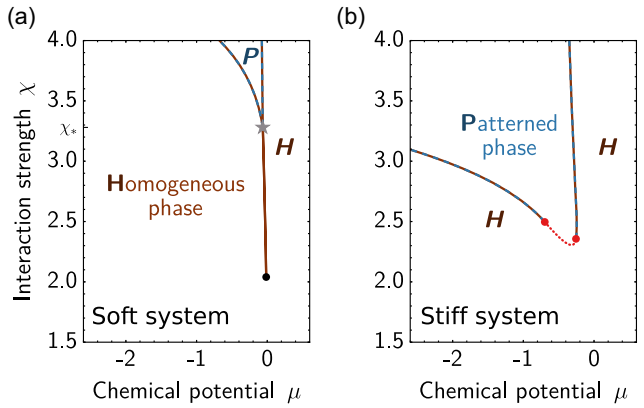

FIG. 2. Grand-canonical phase diagrams reveal patterned phase. (a) Phase diagram as a function of the chemical potential μ and the interaction strength χ for $E = 0.01 k_B T/\nu$. Homogeneous phases (region H) coexist on the brown line between the critical point of phase separation (black disk) and the triple point (gray star), while the patterned phase (region P) coexists with the homogeneous phase on the blue and brown dashed line. (b) Phase diagram as a function of μ and χ for $E = 0.2 k_B T/\nu$. The binodal line separating the homogeneous and patterned phase exhibits either a first-order transition (blue and brown dashed line) or a continuous transition (red dotted line with associated critical points marked by red disks; see details in the Supplemental Material [10]). (a),(b) Model parameters are $\phi_0 = 1$ and $\kappa = 0.05\xi^2$.

To understand when periodic patterns form, we next investigate the simple case where components can freely exchange with a surrounding reservoir kept at fixed chemical potential μ; see Supplemental Material [10]. This situation allows solvent molecules to rush in and out of the system, adjusting the average fraction $\bar{\phi}$ of the elastic component. Figure 2 shows two phase diagrams of this grand-canonical ensemble at different stiffnesses E. In the soft system [Fig. 2(a)], the phase diagram mostly resembles that of ordinary phase separation: For weak interactions ($\chi < 2$), we find only a homogeneous phase and μ simply controls $\bar{\phi}$. In contrast, above the critical point at $\chi \approx 2$ (black disk), we observe a first-order phase transition (brown line) between a dilute phase ($\mu \lesssim 0$) and a dense phase ($\mu \gtrsim 0$). However, at even stronger interactions ($\chi \gtrsim 3.3$), an additional patterned phase (denoted by P) emerges, where the periodic patterns exhibit the lowest free energy. The lines of the first-order phase transitions between the patterned phase and the dilute or dense homogeneous phase (blue and brown dashed curves) meet the line of the phase transition between the two homogeneous states at the triple point (gray star), where these three states coexist.

The grand-canonical phase diagram of soft systems [Fig. 2(a)] qualitatively resembles simple pressure-temperature phase diagrams, e.g., of water. Assuming that the chemical potential μ plays the role of pressure and that the interaction χ is negatively correlated with temperature, the dilute and dense homogeneous phases respectively correspond to the gas and liquid phases. They become indistinguishable at the critical point at low interaction strength (corresponding to high temperatures). In contrast, the patterned phase, with its periodic internal structure, resembles the solid phase.

The general form of the grand-canonical phase diagram persists for stiff systems [Fig. 2(b)], although the parameter region of the patterned phase is much larger. However, the first-order transition between the dilute and dense homogeneous phases disappears together with the normal critical point of phase separation. Instead, we now find a continuous phase transition (dotted red line) between the homogeneous and the patterned phases, which we will discuss in more detail below. Taken together, these phase diagrams suggest that stable patterned phases emerge for sufficiently large stiffness E and interaction χ for intermediated $\bar{\phi}$.

The grand-canonical ensemble that we have discussed so far is suitable when the timescale of an experiment is long compared to the timescale of particle exchange with the reservoir. In the experiments [1], the initial swelling takes place over tens of hours with a measurable increase in size and mass, indicating that solvent soaks the sample until it is equilibrated with the surrounding bath. In contrast, the temperature quench, during which the patterned phase is observed, takes place on a timescale of minutes without the solvent bath. This suggests that this process is better described by a closed system.

D. Patterned and homogeneous phases coexist in closed systems

In the closed system, corresponding to a canonical ensemble, the average fraction $\bar{\phi}$ of elastic components, and thus also the average fraction of solvent, is fixed. In this situation, we find that multiple different phases can coexist in the same system; see Fig. 3. This is again reminiscent of phase separation, where the common-tangent construction reveals the fractions in coexisting homogeneous states. Indeed, we find exactly this behavior in soft systems [left-hand panel of Fig. 3(a)], where a dilute and dense phase coexist for fractions between the two vertical dotted lines, while the free energy of the patterned phase (blue line) is always larger and thus unfavorable. The picture changes for larger stiffness [right-hand panel of Fig. 3(a)], where the patterned phase has lower energy and we can construct two separate common tangents, which respectively connect the dilute and dense homogeneous phase with the patterned phase. Analogously to phase separation, we thus expect situations in which a patterned phase coexists with a homogeneous phase (when $\bar{\phi}$ is in the region marked with $H + P$ or $P + H$). Figure 3(b) corroborates this picture and shows various coexisting phases as a function of the stiffness E and the interaction strength χ. Taken together, the main additional feature of the canonical phase diagrams is the coexistence of multiple phases, which was only

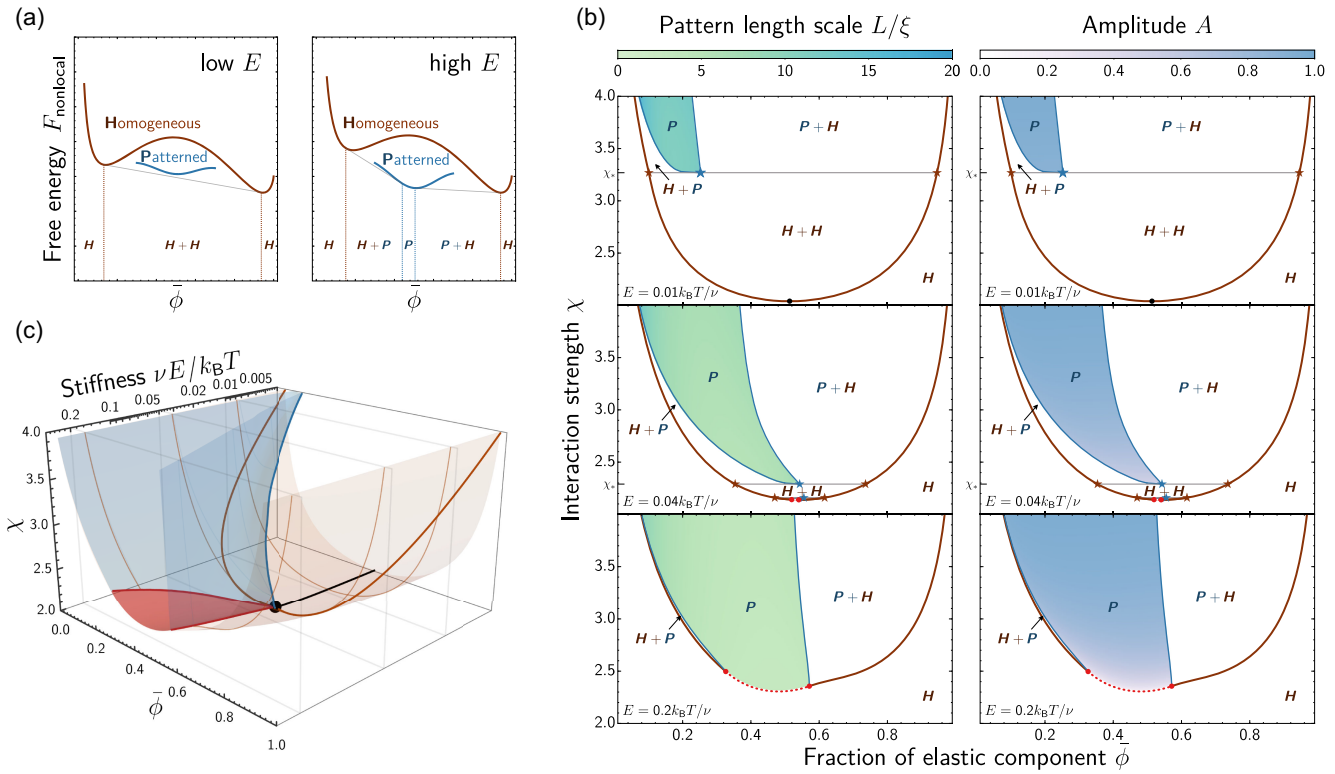

FIG. 3. Closed systems exhibit phase coexistence. (a) Schematic free energy of homogeneous and patterned phases with common-tangent construction (thin gray lines) for two stiffnesses E. Figure S2 in Supplemental Material shows corresponding numerical results [10]. (b) Phase diagram as a function of the average fraction $\bar{\phi}$ of the elastic component and interaction strength χ for various E. Only the homogeneous phase (region H) is stable outside the binodal (brown line; black disk marks critical point) with a continuous phase transition at the red dotted part. Only the patterned phase (region P) is stable inside the blue lines with color codes indicating length scale and amplitude in the left- and right-hand column, respectively. Two indicated phases ($H+P$, $P+H$, $H+H$) coexist in other regions. The triple point corresponds to the tie line (thin gray line), where fractions $\bar{\phi}$ of coexisting homogeneous and patterned phases are marked by brown and blue stars, respectively. (c) Phase diagram as a function of $\bar{\phi}$, χ, and E. The binodal of the homogeneous phase (brown surface) and the patterned phase (blue surface) overlap in the continuous phase transition (red surface). The critical points in (b) now correspond to critical lines, which all merge in the tricritical point (large black disk). A rotating version of the diagram is available as a movie in Supplemental Material [10]. (a)–(c) Model parameters are $\phi_0 = 1$ and $\kappa = 0.05\xi^2$.

possible exactly at the phase transition in the grand-canonical phase diagram.

E. Higher stiffness and interaction strength stabilize patterned phase

The canonical phase diagrams shown in Fig. 3(b) are complex, but they generally preserve three crucial aspects of the grand-canonical phase diagram shown in Fig. 2: Higher stiffness (i) slightly favors the homogeneous phases, (ii) greatly expands the parameter region of the patterned phase, and (iii) induces a continuous phase transition. The first point is illustrated by the binodal line of the homogeneous phase (thick brown lines and red dotted lines), which moves up with increasing stiffness E, implying that larger interaction strengths χ are necessary to stabilize inhomogeneous systems. Inside the binodal line the system exhibits various behaviors, which can be categorized by χ. At a critical value χ_*, the patterned phase (blue star) coexists with the dilute and dense homogeneous phase (brown stars), and the associated tie line corresponds to the triple point in Fig. 2. For weaker interactions ($\chi < \chi_*$), we mostly observe coexistence of a dilute and dense homogeneous phase (region $H+H$), which corresponds to normal phase separation. For stronger interactions ($\chi > \chi_*$), the system exhibits the patterned phase, either exclusively (colored region) or in coexistence with a homogeneous phase (regions $H+P$ and $P+H$). Larger stiffness E lowers the critical value χ_*, thus expanding the parameter region where the patterned phase exists. Eventually, for sufficiently large E, χ_* approaches the critical point of the binodal (gray point), a tiny region with patterned phase appears, and part of the binodal line becomes a continuous phase transition (red dotted line), reproducing the behavior predicted by the grand-canonical phase diagram of stiff systems [Fig. 2(b)].

The influence of stiffness E and interaction strength χ becomes even more apparent in the three-dimensional phase diagram shown in Fig. 3(c): With increasing E, the χ associated with the critical point of phase separation

(black line) increases slightly, whereas the states of three-phase coexistence (blue line and brown lines) shift to lower χ. All lines meet at the tricritical point (black sphere) for $E \approx 0.037 k_B T/\nu$, $\bar{\phi} \approx 0.54$, and $\chi \approx 2.14$. Increasing E further, a part of the binodal line exhibits a continuous phase transition, which expands with larger E. The phase diagram thus summarizes three main aspects of our model. First, the binodal line of phase separation, which is only weakly affected by E, determines whether the system can exhibit nonhomogeneous states. Second, if the system can be inhomogeneous, the stiffness E determines at what value of χ patterned phases emerge. Third, for sufficiently large E, these patterned phases form immediately due to the continuous phase transition.

F. Continuous phase transition explains experimental measurements

The continuous phase transition that we identified at sufficiently large stiffness E implies that the system can change continuously from a homogeneous phase to a patterned phase when the interaction strength χ is increased (corresponding to cooling). Indeed, the amplitude of the predicted pattern vanishes near the transition [right-hand panel of Fig. 3(b)], while the length scale stays finite [left-hand panel of Fig. 3(b)]. This behavior is not expected for typical phase separating systems with first-order transitions, where the order parameter changes discontinuously during the phase transition [see gray line in Fig. 4(a) for an example].

The continuous phase transition was already hypothesized for the experiments [1], based on a lack of hysteresis and a continuous change of the contrast measured by light intensity. To connect to experiments, we mimic the contrast using the square of the amplitude of the optimal volume fraction profile. Figure 4(a) and the right-hand panel of Fig. 3(b) show that the contrast changes continuously from zero when the interaction strength χ is increased for sufficiently stiff systems. Moreover, Fig. 4(b) shows that the associated pattern length scale changes only slightly, consistent with the experiments. Note that deviations in the form of the curves could stem from thermal fluctuations, finite resolution in the experiment, and also deviations in model details.

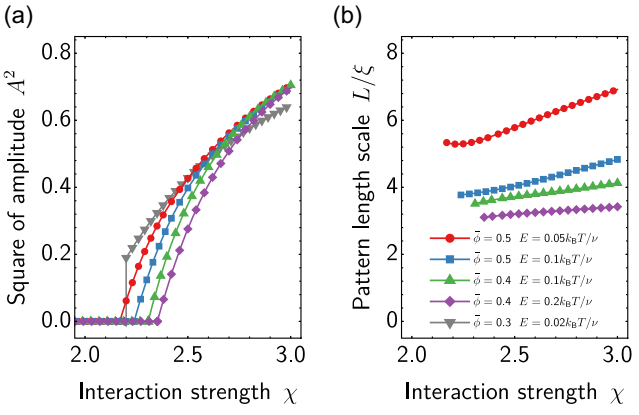

FIG. 4. Continuous phase transition recovers experimental measurements. Squared amplitude (a) and length scale (b) of periodic patterns as a function of interaction strength χ for various parameters indicated in (b), $\phi_0 = 1$, and $\kappa = 0.05\xi^2$. The amplitude indicates a continuous (colored data) and first-order (gray data) transition.

G. Stiffness and interfacial cost control pattern length scale

We next use the numerical minimization of the free energy F_{nonlocal} to analyze how the length scale L of the patterned phase depends on parameters. Figure 5 shows that L decreases with larger stiffness E and increases with the interfacial cost parametrized by κ. The data in Fig. 5(a) suggest the scaling $L/\xi \propto E^{-1/2}$ over a significant parameter range, which matches the experimental observations [1]. Moreover, Fig. 5(b) suggests $L/\xi \propto \xi^{-1/2}\kappa^{1/4}$, which has not been measured experimentally. Taken together, the two scaling laws suggest that the equilibrium length scale emerges from a competition between elastic and interfacial energy.

The two scaling laws emerge qualitatively from a simple estimate of the elastic and interfacial energies: Since shorter patterns have more interfaces, the interfacial energy per unit length is proportional to γL^{-1}, with surface tension $\gamma \propto \kappa^{1/2}$ [23]. In contrast, the elastic energy of a single period originates from stretching a part of material from initial length ξ to final length L, resulting in an elastic energy density proportional to $EL\xi^{-1}$. Minimizing the sum of these two energy densities with respect to L results in $L/\xi \propto \xi^{-1/2}E^{-1/2}\kappa^{1/4}$, which explains the observed scalings qualitatively.

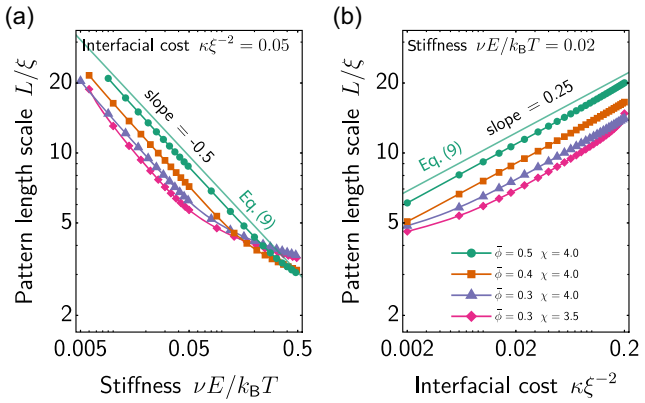

FIG. 5. Pattern length scale exhibits scaling laws. Length scale L as a function of stiffness E (a) and interfacial parameter κ (b) for various parameters. Putative scaling laws are indicated and the prediction by Eq. (9) is shown for $\phi_0 = 1$, $\bar{\phi} = 0.5$, $\chi = 4$, and $\gamma \approx k_B T \kappa^{1/2}/\nu$ (green line).

H. Approximate model predicts length scale

To understand the origin of the length scale L in more detail, we consider the limit of strong phase separation, where the interfacial width is small compared to L; see Fig. 1(c). We thus approximate the volume fraction profile $\phi(x)$ of the elastic component by a periodic step function with fixed fractions ϕ_- and ϕ_+; see dotted lines in Fig. 6(a). Material conservation implies that the relative size of these regions is dictated by the average fraction $\bar{\phi}$ in the swollen state, so we can only vary the period $\tilde{L}$ of the profile. The stable period L then corresponds to the $\tilde{L}$ that minimizes F_{nonlocal} given by Eq. (5), implying $F'_{\text{nonlocal}}(L) = 0$. Since changing $\tilde{L}$ does not affect the local free energy f_0, we investigate only the average free energy of the interface, $\bar{f}_{\text{int}}(\tilde{L}) \approx 2\gamma\tilde{L}^{-1}$, and the average elastic free energy, $\bar{f}_{\text{el}}(\tilde{L}) = \frac{1}{2}\tilde{L}^{-1}\int_0^{\tilde{L}_0}\sigma_{\text{nonlocal}}(X)\epsilon(X)\mathrm{d}X$, where $\tilde{L}_0 = (\bar{\phi}/\phi_0)\tilde{L}$ is the period in the reference frame. Figure 6(b) shows the derivatives of these contributions with respect to $\tilde{L}$, indicating that they sum to zero for $\tilde{L} = L$. We show in the Supplemental Material [10] that

$$\frac{\partial\bar{f}_{\text{el}}}{\partial\tilde{L}} \approx \frac{E}{\xi}\begin{cases} 0 & \tilde{L} < L_{\min} \\ \frac{1}{\sqrt{2\pi}}\left(1-\frac{\bar{\phi}}{\phi_+}\right)^2 & L_{\min} < \tilde{L} < L_{\max} \\ \frac{1}{\sqrt{8\pi}}\left(\frac{\phi_0}{\phi_-}-\frac{\phi_0}{\phi_+}\right)^2\frac{\xi^2}{\tilde{L}^2} & \tilde{L} > L_{\max}, \end{cases} \tag{7}$$

indicating three regimes bounded by

$$L_{\min} = \sqrt{\frac{\pi}{2}}\frac{\phi_0}{\bar{\phi}}\xi \quad \text{and} \quad L_{\max} = \sqrt{\frac{1}{2}}\frac{\phi_0}{\phi_-}\frac{\phi_+-\phi_-}{\phi_+-\bar{\phi}}\xi. \tag{8}$$

Figure 6(b) shows that this approximation of $\partial_{\tilde{L}}\bar{f}_{\text{el}}$ captures the main features of the full numerical data. Figure 6(b) suggests that stable patterns are mainly possible in the gray region ($L_{\min} < \tilde{L} < L_{\max}$), which we interpret further below. In this region, we use Eq. (7) to solve $\partial_{\tilde{L}}\bar{f}_{\text{el}} + \partial_{\tilde{L}}\bar{f}_{\text{int}} = 0$ for $\tilde{L}$, resulting in

$$L \approx (8\pi)^{1/4}\frac{\phi_+}{\phi_+-\bar{\phi}}\left(\frac{\xi\gamma}{E}\right)^{1/2}, \tag{9}$$

consistent with numerical results; see transparent green lines in Fig. 5. This expression shows that the stable period L is governed by the geometric mean of the elastocapillary length γ/E and the nonlocality scale ξ. Moreover, L increases with a larger average fraction $\bar{\phi}$ of the elastic component, i.e., less swelling. In contrast, the fraction ϕ_+ has only a weak influence since it is close to 1 in the case of strong phase separation, implying that the interaction strength χ affects L only weakly.

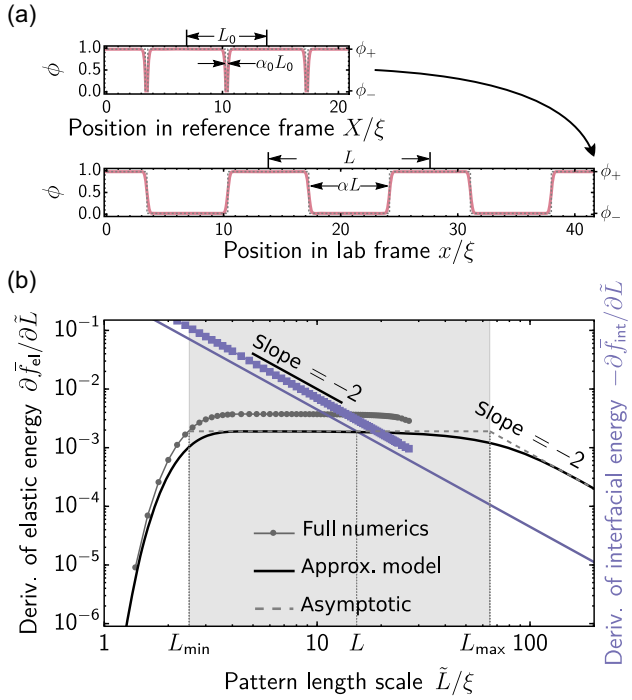

FIG. 6. Approximate model explains scaling laws. (a) Example for a volume fraction profile (pink lines) and the corresponding piecewise approximation (dotted gray lines) in the reference (top) and lab frame (bottom). (b) Derivatives of the average energy density (in units of $k_{\text{B}}T\xi/\nu$) as a function of the pattern period $\tilde{L}$. Shown are data from full numerics (symbols), numerics for the piecewise profile (solid lines), and asymptotic functions (dashed lines) for the elastic (gray, disks) and negative interfacial energy (violet, squares). The stable length L corresponds to the crossing point of the elastic (black) and the interfacial terms (violet). Model parameters are $E = 0.02k_{\text{B}}T/\nu$, $\kappa = 0.05\xi^2$, $\phi_0 = 1$, $\bar{\phi} = 0.5$, and $\chi = 4$.

I. Patterned phase is governed by reference state

Finally, we use the approximate model to understand when the patterned phase emerges. Here, it proves useful to interpret Eq. (8) in the reference frame, where the convolution of the nonlocal elastic energy takes place. Defining the length $L_0 = (\bar{\phi}/\phi_0)L$ in the reference frame and the associated fraction $\alpha_0 = (\phi_-/\phi_0)(\phi_+-\bar{\phi})/(\phi_+-\phi_-)$ occupied by the solvent droplet [Fig. 6(a)], we find

$$L > L_{\min} \Leftrightarrow L_0 > \sqrt{\frac{\pi}{2}}\xi, \tag{10a}$$

$$L < L_{\max} \Leftrightarrow \alpha_0 L_0 < \sqrt{\frac{1}{2}}\xi, \tag{10b}$$

where the numerical prefactors are very close to one. The first condition ($L_0 \gtrsim \xi$) suggests that two solvent droplets need to be separated by more than ξ in the reference frame since L_0 roughly estimates their separation; see Fig. 6(a). If droplets were closer, they would feel each other's deformations, which is apparently unfavorable. In the extreme case

($L_0 \ll \xi$), the average elastic energy is almost constant, essentially because short-ranged variations are averaged by the comparatively large nonlocal kernel. In contrast, the second condition implies that the droplet size in the reference frame ($\alpha_0 L_0$) must be smaller than the nonlocality scale ξ. Assuming ξ corresponds to the mesh correlation length, this suggests that the droplet can at most deform the correlated part of the mesh, which we will discuss below. If droplets were larger ($\alpha_0 L_0 \gg \xi$), nonlocal features would only be relevant at interfaces, so the system would behave as if it had only local elasticity and coarsen indefinitely.

This analysis highlights that the existence of the periodic pattern depends on the reference frame, while its length scale L also depends on the different stretch of the dilute and dense region; see Fig. 6(a). This observation suggests an intuitive explanation for the influence of the interaction χ: Assuming that ϕ_- and ϕ_+ correspond to equilibrium volume fractions and $\bar{\phi} = \frac{1}{2}$ for simplicity, we find $\alpha_0 \propto \phi_-$, which decreases with larger χ. Consequently, the lower bound $L_{\min}$ is unaffected, while $L_{\max}$ increases, consistent with our observation that the patterned phase forms easier at higher χ and the scaling law given by Eq. (9) holds for broader parameter range with higher interaction strength (Fig. 5).

J. Spatial heterogeneity could cause nonlocality

Since the periodic equilibrium patterns crucially depend on the nonlocality scale ξ, we hypothesize that such a length scale is relevant in the experiments [1]. However, it is unlikely that the mesh size (typically below 100 nm) directly controls ξ since the observed droplets are larger (several hundred nanometers). Instead, we propose that ξ is governed by spatial heterogeneities. The correlation length of these heterogeneities, roughly measuring the size of soft regions, can be much larger than the mesh size [27–29]. Figure 7 illustrates the difference between the two interpretations.

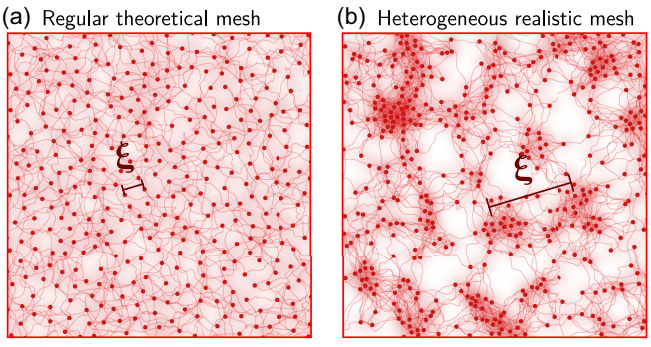

FIG. 7. Heterogeneity could explain nonlocality scale ξ. (a) Schematic of a relatively regular mesh, whose nonlocality scale ξ is linked to the mesh size. (b) Schematic of a heterogeneous mesh, where ξ is given by the correlation length of spatial heterogeneities.

Realistic meshes exhibit multiple length scales, which could all affect the behavior. To elucidate this, we briefly consider the impact of a convolution kernel that consists of two parts, $g(X) = (1-\zeta)g_{\xi_1}(X) + \zeta g_{\xi_2}(X)$, where ξ_1 represents the mesh size, ξ_2 denotes the scale of spatial heterogeneities, and the nondimensional weight $\zeta < 1$ determines the relative contributions. If the mesh size ξ_1 is much smaller than the pattern length scale, the corresponding convolution reduces to local elasticity, so the elastic energy following from Eq. (3) can be approximated as

$$F_{\mathrm{el}} \approx \frac{(1-\zeta)E}{2} \int \epsilon(X)^2 \mathrm{d}X + \frac{\zeta E}{2} \iint \epsilon(X)\epsilon(X') g_{\xi_2}(X-X') \mathrm{d}X \mathrm{d}X'. \quad (11)$$

The part corresponding to ξ_1 effectively changes only the local free-energy density. In the simple case of one-dimensional systems, the first integrand can then be expressed in terms of the volume fraction ϕ, and absorbed in a rescaled free-energy density $f_0(\phi)$. In contrast, the nonlocality scale ξ_2 provided by the second term will control the periodic equilibrium patterns. The effective stiffness corresponding to this term is ζE, whereas the experimentally measured bulk modulus of a uniform deformation will include both terms and thus remain E. Taken together, this increases the effective elastocapillary length to $\gamma/(\zeta E)$, implying larger pattern length scales L; see Eq. (9).

III. DISCUSSION

We propose a phenomenological theory that explains the experimentally observed patterns [1] based on nonlocal elasticity, which captures aspects of the mesh's structure. Within our equilibrium theory, regular periodic patterns appear for sufficiently strong phase separation (large enough χ) and stiffness E, while surface tension γ opposes the trend. Essentially, solvent droplets inflate a region of the elastic mesh of the size of the nonlocality scale ξ. The pattern period L then results from a balance of elastic and interfacial energies, so that L scales as the geometric mean between ξ and the elastocapillary length γ/E. In contrast, the interaction strength χ, leading to phase separation in the first place, affects L only weakly, but it determines whether the patterned phase is stable, similar to ordinary phase separation. However, the transition between the homogeneous and heterogeneous phase, which is normally first order, can now be continuous. Consequently, the patterned phase can appear with arbitrarily small amplitude in a reversible process.

Our model captures the main features of the experiment [1], including the continuous phase transition leading to reversible dynamics. This suggests that the experiment is in quasiequilibrium, which would also explain why the pattern is independent of the cooling rate. Moreover, our theory explains why the pattern length scale L is only

weakly affected by the final temperature and decreases with stiffness E. Importantly, our model predicts that a structural length ξ of the mesh is essential for the emergence of the observed L. Our numerics indicate that L can be an order of magnitude larger than ξ, suggesting that ξ could relate to observed correlation lengths of the order of a few hundred nanometers [27]. Since ξ is small compared to the distance between droplets [see Eq. (10)], the nonlocal effects of elasticity do not affect droplet positioning. Furthermore, we found that a coexisting homogeneous phase does not affect the free energy of the patterned phase strongly (see Supplemental Material [10]), suggesting that the two phases can be interspersed, which would contribute to irregularity of the droplet placement in real systems. In contrast, the observed variation in droplet size [1] likely originates from local heterogeneity in material properties, like ξ, E, and γ.

To capture the mesh's structure, we employ nonlocal elasticity [18–22] based on a convolution of the strain field. Such nonlocal elasticity emerges naturally for phenomenological theories and from coarse-graining microscopic theories. The description only converges to local elasticity theory when the length scales of phenomena are large compared to the nonlocality scale. While such length scale separation is often feasible in macroscopic elastic problems, nonlocal elasticity is required to explain microscopic phenomena, e.g., in fracture mechanics [35]. Indeed, the convolution kernel given by Eq. (4) can be interpreted as a Green's function of a diffusion process in the reference frame, suggesting that the nonlocal elasticity is similar to the damage field introduced in fracture mechanics [36]. Taken together, nonlocal elasticity theories are crucial to describe elastic phenomena in microscopic systems, e.g., biological cells.

Our work complements related theories of phase separation in elastic media, which either modeled pores explicitly [26,37–40] or resorted to particle-based methods [41,42]. Nonlocality is generally responsible for the emergence of structure in multiple physical systems, such as the Ohta-Kawasaki model [43], phase separation with electrostatic interaction [44], and also nonlocal elasticity [45,46], e.g., to study polymeric materials [47,48]. However, in the first two models, the convolution acts directly on the described field ϕ, whereas we convolved the strain field ϵ, which is inversely related to ϕ; see Eq. (2). Moreover, the Coulomb form of the convolution kernel prohibits macrophase separation in these two models. Another difference is that we use a convolution in the reference frame, capturing the quenched microscopic topology of the elastic mesh. These differences are a consequence of the fact that we build our phenomenological model systematically for the case of elastic meshes.

We developed our model for the simple case of one spatial dimension, which surprisingly already accounts for the key experimental observations. However, to capture more details, including various morphologies, we will need to generalize the model to higher dimensions, which will require a tensorial convolution kernel [19]. Additionally, nonlocal elasticity can be viewed as a phenomenological model containing the correlation length of spatial heterogeneities of the polymer network [49]. In realistic meshes, heterogeneities would imply disorder in the convolution kernel, but our theory suggests that only the long-range behavior is crucial for forming patterns. More generally, disorder might affect the phase transition and the morphologies of patterns, potentially explaining the lack of long-range order. Incorporating quenched disorder would require a proper averaging based on statistical mechanics, e.g., by applying a random convolution kernel or combining simulation techniques [49,50]. Moreover, to describe details of the experiments, we might require more realistic models of phase separation (including different molecular sizes and higher-order interactions terms) and elasticity (involving finite extensibility, viscoelasticity [51], as well as plastic deformation, like fracture [52,53] and cavitation, which can lead to regular droplet patterns [54]). Finally, experimental systems exhibit heterogeneities in key model parameters including ξ, E, and γ, which will contribute to uncertainty and might even induce large-scale rearrangements [9,55]. Such extended theories will allow us to compare the full pair correlation and scattering functions to experiments, shedding light on how we can manipulate this pattern forming system to control microstructures.

ACKNOWLEDGMENTS

We thank Carla Fernández-Rico, Robert W. Style, Eric R. Dufresne, Marcus Müller, and Stefan Karpitschka for helpful discussions. We gratefully acknowledge funding from the Max Planck Society and the European Union (ERC, EmulSim, 101044662).

[1] C. Fernández-Rico, S. Schreiber, H. Oudich, C. Lorenz, A. Sicher, T. Sai, V. Bauernfeind, S. Heyden, P. Carrara, L. D. Lorenzis, R. W. Style, and E. R. Dufresne, *Elastic microphase separation produces robust bicontinuous materials*, Nat. Mater. **23**, 124 (2024).

[2] C. Fernández-Rico, T. Sai, A. Sicher, R. W. Style, and E. R. Dufresne, *Putting the squeeze on phase separation*, JACS Au **2**, 66 (2022).

[3] R. W. Style, T. Sai, N. Fanelli, M. Ijavi, K. Smith-Mannschott, Q. Xu, L. A. Wilen, and E. R. Dufresne, *Liquid-liquid phase separation in an elastic network*, Phys. Rev. X **8**, 011028 (2018).

[4] D. S. W. Lee, A. R. Strom, and C. P. Brangwynne, *The mechanobiology of nuclear phase separation*, APL Bioeng. **6**, 021503 (2022).

[5] T. J. Böddeker, K. A. Rosowski, D. Berchtold, L. Emmanouilidis, Y. Han, F. H. T. Allain, R. W. Style, L. Pelkmans, and E. R. Dufresne, *Non-specific adhesive forces between filaments and membraneless organelles*, Nat. Phys. **18**, 571 (2022).

[6] D. S. W. Lee, N. S. Wingreen, and C. P. Brangwynne, *Chromatin mechanics dictates subdiffusion and coarsening*

dynamics of embedded condensates, Nat. Phys. **17**, 531 (2021).
[7] F. S. Bates, M. A. Hillmyer, T. P. Lodge, C. M. Bates, K. T. Delaney, and G. H. Fredrickson, *Multiblock polymers: Panacea or Pandora's box?*, Science **336**, 434 (2012).
[8] Q. Tran-Cong and A. Harada, *Reaction-induced ordering phenomena in binary polymer mixtures*, Phys. Rev. Lett. **76**, 1162 (1996).
[9] K. A. Rosowski, T. Sai, E. Vidal-Henriquez, D. Zwicker, R. W. Style, and E. R. Dufresne, *Elastic ripening and inhibition of liquid-liquid phase separation*, Nat. Phys. **16**, 422 (2020).
[10] See Supplemental Material at http://link.aps.org/supplemental/10.1103/PhysRevX.14.021009 for theoretical details of the model, numerical methods for minimizing the free energy as well as constructing phase diagrams, and supplemental figures.
[11] S. Foerster, A. K. Khandpur, J. Zhao, F. S. Bates, I. W. Hamley, A. J. Ryan, and W. Bras, *Complex phase behavior of polyisoprene-polystyrene diblock copolymers near the order-disorder transition*, Macromolecules **27**, 6922 (1994).
[12] M. W. Matsen, *The standard Gaussian model for block copolymer melts*, J. Phys. Condens. Matter **14**, R21 (2001).
[13] R. M. Briber and B. J. Bauer, *Effect of crosslinks on the phase separation behavior of a miscible polymer blend*, Macromolecules **21**, 3296 (1988).
[14] I. Alig, M. Junker, M. Schulz, and H. L. Frisch, *Irreversible frustrated spinodal decomposition in simultaneous interpenetrating polymer networks: Small-angle x-ray scattering*, Phys. Rev. B **53**, 11481 (1996).
[15] K. Yamada, M. Nonomura, and T. Ohta, *Kinetics of morphological transitions in microphase-separated diblock copolymers*, Macromolecules **37**, 5762 (2004).
[16] A. Onuki and S. Puri, *Spinodal decomposition in gels*, Phys. Rev. E **59**, R1331 (1999).
[17] O. Peleg, M. Kröger, and Y. Rabin, *Model of microphase separation in two-dimensional gels*, Macromolecules **41**, 3267 (2008).
[18] I. A. Kunin, in *Elastic Media with Microstructure I*, edited by E. Kröner, M. Cardona, P. Fulde, and H.-J. Queisser, Springer Series in Solid-State Sciences, Vol. 26 (Springer, Berlin, 1982), 10.1007/978-3-642-81748-9.
[19] I. A. Kunin, in *Elastic Media with Microstructure II*, edited by E. Kröner, M. Cardona, P. Fulde, and H.-J. Queisser, Springer Series in Solid-State Sciences, Vol. 44 (Springer, Berlin, 1983), 10.1007/978-3-642-81960-5.
[20] A. C. Eringen, *Vistas of nonlocal continuum physics*, Int. J. Eng. Sci. **30**, 1551 (1992).
[21] *Nonlocal Continuum Field Theories*, edited by A. C. Eringen (Springer, New York, 2004), 10.1007/b97697.
[22] R. Maranganti and P. Sharma, *Length scales at which classical elasticity breaks down for various materials*, Phys. Rev. Lett. **98**, 195504 (2007).
[23] J. W. Cahn and J. E. Hilliard, *Free energy of a nonuniform system. I. Interfacial free energy*, J. Chem. Phys. **28**, 258 (1958).
[24] C. A. Weber, D. Zwicker, F. Jülicher, and C. F. Lee, *Physics of active emulsions*, Rep. Prog. Phys. **82**, 064601 (2019).
[25] N. R. Richbourg and N. A. Peppas, *The swollen polymer network hypothesis: Quantitative models of hydrogel swelling, stiffness, and solute transport*, Prog. Polym. Sci. **105**, 101243 (2020).
[26] P. Ronceray, S. Mao, A. Košmrlj, and M. P. Haataja, *Liquid demixing in elastic networks: Cavitation, permeation, or size selection?*, Europhys. Lett. **137**, 67001 (2022).
[27] K. Saalwächter and S. Seiffert, *Dynamics-based assessment of nanoscopic polymer-network mesh structures and their defects*, Soft Matter **14**, 1976 (2018).
[28] S. Seiffert, *Origin of nanostructural inhomogeneity in polymer-network gels*, Polym. Prepr. **8**, 4472 (2017).
[29] P. Malo de Molina, S. Lad, and M. E. Helgeson, *Heterogeneity and its influence on the properties of difunctional poly(ethylene glycol) hydrogels: Structure and mechanics*, Macromolecules **48**, 5402 (2015).
[30] S. Gopalakrishnan and S. Narendar, *Wave Propagation in Nanostructures: Nonlocal Continuum Mechanics Formulations*, NanoScience and Technology (Springer International Publishing, Cham, Switzerland, 2013), 10.1007/978-3-319-01032-8.
[31] P. D. Wu and E. Van Der Giessen, *On improved network models for rubber elasticity and their applications to orientation hardening in glassy polymers*, J. Mech. Phys. Solids **41**, 427 (1993).
[32] P. J. Flory, *Thermodynamics of high polymer solutions*, J. Chem. Phys. **10**, 51 (1942).
[33] M. L. Huggins, *Solutions of long chain compounds*, J. Chem. Phys. **9**, 440 (1941).
[34] P. J. Flory, *Statistical mechanics of swelling of network structures*, J. Chem. Phys. **18**, 108 (1950).
[35] A. C. Eringen, C. G. Speziale, and B. S. Kim, *Crack-tip problem in non-local elasticity*, J. Mech. Phys. Solids **25**, 339 (1977).
[36] B. Bourdin, G. A. Francfort, and J.-J. Marigo, *The variational approach to fracture*, J. Elast. **91**, 5 (2008).
[37] M. Kothari and T. Cohen, *The crucial role of elasticity in regulating liquid-liquid phase separation in cells*, Biomech. Model Mechanobiol. **22**, 645 (2023).
[38] J. Little, A. J. Levine, A. R. Singh, and R. Bruinsma, *Finite-strain elasticity theory and liquid-liquid phase separation in compressible gels*, Phys. Rev. E **107**, 024418 (2023).
[39] S. Biswas, B. Mukherjee, and B. Chakrabarti, *Thermodynamics predicts a stable microdroplet phase in polymer-gel mixtures undergoing elastic phase separation*, Soft Matter **18**, 8117 (2022).
[40] X. Wei, J. Zhou, Y. Wang, and F. Meng, *Modeling elastically mediated liquid-liquid phase separation*, Phys. Rev. Lett. **125**, 268001 (2020).
[41] T. Curk and E. Luijten, *Phase separation and ripening in a viscoelastic gel*, arXiv:2201.08922.
[42] Y. Zhang, D. S. W. Lee, Y. Meir, C. P. Brangwynne, and N. S. Wingreen, *Mechanical frustration of phase separation in the cell nucleus by chromatin*, Phys. Rev. Lett. **126**, 258102 (2021).
[43] T. Ohta and K. Kawasaki, *Equilibrium morphology of block copolymer melts*, Macromolecules **19**, 2621 (1986).
[44] C. B. Muratov, *Theory of domain patterns in systems with long-range interactions of Coulomb type*, Phys. Rev. E **66**, 066108 (2002).

[45] X. Ren and L. Truskinovsky, *Finite scale microstructures in nonlocal elasticity*, in *Advances in Continuum Mechanics and Thermodynamics of Material Behavior*, edited by D. E. Carlson and Y.-C. Chen (Springer Netherlands, Dordrecht, 2000), pp. 319–355, 10.1007/978-94-010-0728-3_18.

[46] O. W. Paulin, L. C. Morrow, M. G. Hennessy, and C. W. MacMinn, *Fluid–fluid phase separation in a soft porous medium*, J. Mech. Phys. Solids **164**, 104892 (2022).

[47] S. Heyden, S. Conti, and M. Ortiz, *A nonlocal model of fracture by crazing in polymers*, Mech. Mater. **90**, 131 (2015).

[48] S. Nikolov, C. S. Han, and D. Raabe, *On the origin of size effects in small-strain elasticity of solid polymers*, Int. J. Solids Struct. **44**, 1582 (2007).

[49] X. Mao, P. M. Goldbart, X. Xing, and A. Zippelius, *Soft random solids and their heterogeneous elasticity*, Phys. Rev. E **80**, 031140 (2009).

[50] G. Wang, A. Zippelius, and M. Müller, *Phase separation of randomly cross-linked diblock copolymers*, Macromolecules **55**, 5567 (2022).

[51] H. Tanaka, *Viscoelastic phase separation in biological cells*, Commun. Phys. **5**, 1 (2022).

[52] J. Y. Kim, Z. Liu, B. M. Weon, T. Cohen, C.-Y. Hui, E. R. Dufresne, and R. W. Style, *Extreme cavity expansion in soft solids: Damage without fracture*, Sci. Adv. **6**, eaaz0418 (2020).

[53] S. Raayai-Ardakani, D. R. Earl, and T. Cohen, *The intimate relationship between cavitation and fracture*, Soft Matter **15**, 4999 (2019).

[54] E. Vidal-Henriquez and D. Zwicker, *Cavitation controls droplet sizes in elastic media*, Proc. Natl. Acad. Sci. U.S.A. **118**, e2102014118 (2021).

[55] E. Vidal-Henriquez and D. Zwicker, *Theory of droplet ripening in stiffness gradients*, Soft Matter **16**, 5898 (2020).